Magnetic structure and dynamics of surface-spin systems of the 3d transition metal monoxides studied by metastable helium beam scattering

2002 J. Phys.: Condens. Matter 14 6281

(http://iopscience.iop.org/0953-8984/14/24/319)

INSTITUTE OF PHYSICS PUBLISHING JOURNAL OF PHYSICS: CONDENSED MATTER

J. Phys.: Condens. Matter **14** (2002) 6281–6306 PII: S0953-8984(02)36388-4

Magnetic structure and dynamics of surface-spin systems of the 3d transition metal monoxides studied by metastable helium beam scattering

M El-Batanouny

Department of Physics, Boston University, 590 Commonwealth Ave., Boston, MA 02215, USA

Received 30 April 2002
Published 31 May 2002

Abstract

The application of diffractive and inelastic surface scattering of coherent 2^3S metastable helium beams (He*) to study the physics of surface antiferromagnetic (AFM) properties of insulators, in particular, of the 3d monoxides, is presented. First, we discuss the sensitivity of the scattering process to surface spin-ordering and dynamics, and introduce the experimental methodology for its implementation. A brief discussion of our current understanding of surface magnetic critical behaviour, and of the known bulk properties of the 3d transition metal monoxides is then given. Finally, recent experimental and theoretical results are presented. Foremost among these results are the observation of an extraordinary surface AFM transition on NiO(001), measurement of dispersive surface AFM excitonic waves and the observation of re-entrant-like, anomalous temperature enhancement of the sublattice magnetization on CoO(001).

1. Introduction

The scattering of light noble gas atomic beams from surfaces has proven to be a very useful technique for determining structural and dynamical properties of the surface atomic lattice. In this capacity helium atom scattering (HAS) is the archetypical example. Elastic helium atom scattering (EHAS) has provided valuable information about surface structures, surface defects and about the growth of ultra-thin films [1]. Inelastic helium atom scattering (IHAS) has played a leading role over the past decade in revealing unprecedented information about the dynamics of solid surfaces, ranging from surface phonon dispersion curves to diffusion and the dynamics of surface melting [2]. Theoretical modelling of the scattering of He atoms from solid surfaces has followed two approaches: one adopts the semi-classical framework of the eikonal approximation [3,4], and the other a quantum mechanical formulation based on the Born approximation [5]. Inelastic scattering of He atoms, involving interaction with the surface vibrations, was treated by Manson and Celli using a distorted-wave Born approximation (DWBA) approach [6–8].

In this review I discuss how the technique of surface scattering of metastable 2^3S helium atoms (He*) can extend these studies to the physics of long-range antiferromagnetic (AFM) surface-spin ordering and its dynamics. As an example, I present recent results obtained for the (001) surfaces of NiO and CoO. These two systems exhibit several similarities: they have the same crystal structure, their lattice constants only differ by about 1%, their (001) surfaces do not reconstruct and the (001) AFM ordering is (2×1), which is just the expected termination of bulk ferromagnetic (FM) (111)-sheets with AFM stacking. Yet, they present quite contrasting critical behaviour: it was found that NiO(001) is the first known system to exhibit a surface *extraordinary* transition [9], while CoO(001) presents an anomalous enhancement of its surface AFM sublattice magnetization (SLM) with temperature increase [10].

Currently, we have a thorough understanding of the bulk magnetic properties of the family of AFM 3d monoxide crystals, MnO, FeO, CoO and NiO, with the rock-salt structure, based on extensive studies of these systems over the past five decades [11–27]. Experimental studies, mainly involving thermal neutron scattering, provided valuable information about their long-range spin ordering, spin dynamics and spin-wave dispersion, and the critical behaviour of the SLM. This was paralleled by a host of theoretical studies that elucidated our understanding of the basic physics underlying both their critical behaviour and dynamics.

By contrast, our understanding of the physics of surface magnetic properties, in general, has been lagging both experimentally and theoretically. From the experimental side, it is attributed to the unavailability of an adequate surface probe capable of providing the relevant information. Theoretical studies of surface magnetic effects have been scarce and less forthcoming because of the lack of the stimulus of experimental results. Instead, attention was devoted to bulk magnetic behaviour, and surface effects on bulk critical behaviour have been ignored. The argument has been advanced that surface effects will be appreciable only within a bulk correlation length, which for all practical reasons is always much smaller than the physical size of the systems studied since experimentally attainable correlation lengths are of the order of a few thousand angstroms.

Theoretical studies of surface critical behaviour of magnetic systems had a late start [28–48]. They were spurred by LEED results of a 2×1 AFM structure on NiO(001), reported by Palmberg *et al* in 1968–1971 [29, 49, 50]. It was then recognized that the factors that influence surface critical behaviour are split into two main categories: The first category consists of 'geometric' effects involving the breaking of translational symmetry, the reduction of rotational symmetries and missing neighbours. The second category consists of 'dynamical' effects manifested by the fact that magnetic interactions at the surface may be quite different from those in the bulk. This raised the possibility that the surface may order before the bulk if the effective surface interactions are stronger than those in the bulk. The thermodynamic average of an observable localized at the surface will, in general, be different from its value deep in the bulk; for example, the local magnetization m_1 at the surface will differ from the bulk magnetization m_b. Correlation functions involving spins at the surface are also expected to be strongly modified. These changes made it necessary to introduce new exponents to describe the critical behaviour at the surface, for example the exponent β_1 for the surface magnetization. As a consequence of such changes, it was argued that surface magnetic properties may exhibit a rich phase diagram. Initially, our understanding of these effects was largely based on mean-field theory (MFT) and on the phenomenological theory of scaling (PTS), despite their known shortcomings in predicting the values of the critical exponents [28–32, 36, 38, 39, 46]. Although important information has also come from exact solutions [36], series analysis [30, 31], Monte Carlo (MC) calculations [33–35, 44, 45, 48] and more recently field-theoretic methods [40–43, 47, 51], the primary role of these latter techniques was to confirm or refine the physical ideas that had been put forward by MFT and PTS.

MFT predicts three possible regimes for surface critical behaviour. When the effective surface exchange interaction (J_s) is weaker than a critical value (J_s^c) the surface is forced to order at the bulk transition temperature (T_c^b), and the ensuing transition is labelled *ordinary* [46]. However, when $J_s = J_s^c$, the surface orders at T_c^b, independent of the bulk, a multi-critical behaviour labelled a *surface special* transition [38]. When $J_s > J_s^c$, a purely two-dimensional transition takes place at a temperature $T_c^s > T_c^b$, and a crossover to MC behaviour at T_c^b. The latter has been coined an *extraordinary* transition [46]. But MFT is known to be incorrect for bulk properties near T_c^b when the space dimension is below the upper critical value, $d^* = 4$, for short range interactions. MFT wrongly predicts that bulk critical exponents are independent of the dimensionality of the order parameter. A similar breakdown of MFT should occur for local critical properties. For example, although MFT provides a correct qualitative description of the surface critical behaviour of a three-dimensional semi-infinite Ising model, it gives the wrong prediction for the surface critical behaviour of the two-dimensional Ising system. Moreover, recent field-theoretic analyses have shown that the surface exponents cannot in general be expressed completely in terms of bulk exponents [43], contrary to arguments and predictions based on scaling theory [38, 52].

Further experimental activity concerning surface Magnetic ordering and its critical behaviour only resumed in the eighties, and was limited to FM metallic systems. SPLEED studies of Ni(001) and Ni(110) [53, 54] reported a behaviour consistent with an ordinary transition. Experimental studies of the 4f Gd(0001) FM surface, employing the techniques of electron capture spectroscopy (ECS) and SPLEED, reported enhancements in surface magnetic transition temperature T_c^s ranging from 15 to 60 K [55–58]. ECS and SPLEED results showed an anomalous peak in magnetic-scattering intensities that appear above T_c^b, which was first attributed to a possible AFM coupling to the bulk, and subsequently identified with the component parallel to the surface, with an FM orientation with respect to the bulk magnetization [58]. These studies also reported the presence of a component in the surface magnetization normal to the surface. However, because of such complicating features, the nature of the critical behaviour could not be discerned. Another 4f system whose magnetic critical behaviour was studied is Tb(0001) [59]. It was found that the surfaces of thick films of Tb underwent a Curie T_c^s higher than the Néel and Curie temperatures of its bulk; moreover, the critical behaviour of this transition was consistent with that of the semi-infinite anisotropic Heisenberg system.

Recently, magnetic He* atom scattering (MHAS) opened up the possibility of investigating surface AFM critical behaviour experimentally. The de Broglie wavelength of He* atoms at thermal kinetic energies is compatible with surface diffraction, and the classical scattering turning points occur at 3–4 Å in front of the crystal surface. Consequently, this technique is exclusively surface sensitive. It was also demonstrated that He* diffraction is highly sensitive to surface AFM ordering [60–64]. Moreover, in contrast to LEED, it does not suffer from limitations imposed by surface charging effects. Recent measurements on NiO(001) surfaces, cleaved in vacuum, consistently showed a (2 × 1) AFM-ordering of the surface electron spin structure with a surface Néel temperature T_N^s of 529 K, higher than the bulk value of $T_N^b = 523.6$ K [9]. Furthermore, analysis of its critical behaviour revealed the first observation of a crossover behaviour consistent with the class of the anisotropic extraordinary transition of the semi-infinite Heisenberg model [65], which is very similar to the semi-infinite Ising model [33–35]. By contrast, more recent studies of CoO(001) showed a similar 2 × 1 AFM surface structure. However, it revealed a quite novel critical behaviour characterized by an anomalous enhancement in the magnetic 1/2-order peak intensity which straddles T_N^b, yet exhibits a pronounced suppression at T_N^b.

In section 2 the principles of He* scattering from magnetic surfaces are discussed, and a brief outline of its formulation within the eikonal and DWB approximations is given. In section 3 the details of the experimental facility and procedures are presented. For the sake of completeness, section 4 highlights important aspects of magnetic critical behaviour at surfaces. Section 5 contains an outline of relevant surface and bulk properties of 3d monoxides. It also presents results of extensive configuration interaction cluster calculations of the surface electronic structure of NiO(001) and CoO(001). In section 6 results and discussion of the NiO(001) and CoO(001) systems are presented.

2. Scattering of He* beams from magnetic surfaces: principles and formalism

The lowest-lying excited state of atomic He is a metastable triplet 2^3S, with an excitation energy of 19.8 eV. It has the longest known lifetime of any atomic metastable state, $\sim 10^4$ s [66–68], since spontaneous decay to the ground state (GS) must involve a two-photon transition and a spin-flip. The second lowest excited state of He is a metastable singlet 2^1S with excitation energy of 20.6 eV and a lifetime of 2×10^{-2} s [66–68]. The techniques discussed here are based solely on the properties of the triplet metastable state, which hereafter is exclusively referred to as He*. Moreover, since He* atoms at thermal energies travel with a velocity of about 1.7 km s^{-1}, the transit time from source to sample over a typical distance of $\simeq$0.5–0.25 m is less than a millisecond, much shorter than its lifetime.

Although the He* state is very long lived in vacuum, it readily decays to the GS upon impact with atoms, molecules and most surfaces. Conrad *et al* [69] measured survival probabilities 10^{-3}–10^{-6} for thermal energy He* atoms incident on clean metal surfaces, and 10^{-4} on insulator surfaces.

2.1. Decay channels

There exist two predominant interaction channels that allow a He* atom to decay to its GS as it approaches a surface: resonance ionization/Auger neutralization (RIAN) and Penning de-excitation (PD) [69–72]. The former process, shown in figure 1(a), takes place when the excited He 2s orbital is degenerate with an unoccupied local density of surface electronic states. In that case, as the He* atom approaches the surface, it is first ionized by tunnelling of the 2s electron into an available degenerate empty surface state. The resulting He$^+$ ion continues to travel towards the surface where it is neutralized through an Auger process in which an electron from the surface with appropriate spin orientation fills the 1s hole of the He atom. The energy released in this process is imparted to a second surface electron. For most magnetic insulators, and especially the 3d monoxides, the energy level of the 2s orbital falls in the insulating gap, and this process is inhibited. The PD process, shown in figure 1(b), prevails in this case, and the decay then occurs via an Auger process involving a surface electron, with the appropriate spin orientation, and the 2s He* electron. In this process the surface electron fills the 1s He hole and the energy released is taken up by the 2s electron.

Note that de-excitation processes involving internal spin-flips of the 2s electron (i.e. converting the triplet into a singlet configuration) are energetically unfavourable and require high order processes because the excitation energy of the singlet is almost 1 eV greater than that of the triplet.

2.2. Selection rules and magnetic diffraction

When the 2s He* electron state lies within the energy gap of a magnetic insulator, only PD can take place. If we take the polarization of the He* atom to be ‘up’, then the Pauli exclusion principle requires the spin polarization of the surface electron involved in the Auger de-excitation process to be ‘down’. Therefore, only surface electrons with ‘down’ spin polarization

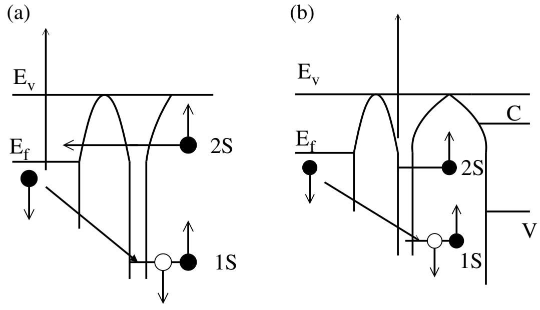

Figure 1. (a) RIAN process. (b) PD process.

can contribute to this decay process, and the survival probability will depend on the *relative orientations* of the spins of the He* 2s electron and the local surface electron: a He* atom will be more likely to survive scattering if its spin orientation is parallel to the local surface electron spins, but will be more likely to decay to the GS if the spins are antiparallel. Accordingly, if the orientations of the local moments on the surface are arranged periodically, the beam attenuation should exhibit a periodic modulation, that will be reflected in the diffraction pattern of the elastically scattered He* atoms. Thus, diffractive He* scattering reflects the surface spin ordering as well as the geometric surface structure.

As an example, we consider what will happen to a beam of He* incident upon the *ideal* AFM surface, shown in figure 2, where the spin-orientation of the electrons on the A sublattice sites is parallel to that of the He*, while the electrons on the B sublattice sites have antiparallel spin-orientation to that of He*. Then all of the He* that strike B sites will decay to the GS, whereas He* that strike A sites will survive the scattering event and yield a diffraction pattern reflecting the periodicity of surface spin-ordering. This process is analogous to light scattering from a reflective grating: light which strikes the slits in the grating is lost, while the reflected light is diffracted. If the incident He* beam is unpolarized, the diffractively scattered He* will still reflect the periodicity of the surface spin-ordering, but no information about the absolute spin direction of the lattice will be provided.

2.3. Modelling the dissipative potential

Of course, on a real AFM surface, majority and minority spins will be present at all sites, and thus the He* beam will experience attenuation at all sites. However, if the surface sites have a net spin, the attenuation of the He* beam will be periodically modulated, and the resulting diffraction pattern will again reflect the periodicity of the surface spin-ordering. Consequently, the attenuation of the He* beam upon scattering from AFM surfaces can be taken into account by introducing an imaginary part to the scattering potential, comprised of (i) a spatially uniform background

$$V_0 = C_0 \mathcal{M}_{\mathrm{Aug}} \mathcal{D}_0, \tag{1}$$

where $\mathcal{M}_{\mathrm{Aug}}$ is the Auger matrix element of the PD process, $\mathcal{D}_0$ is an average background surface electron local density of states (LDOS) available for the PD decay and C_0 encompasses all remaining constants, and (ii) a spatial- and spin-dependent term, ΔV^S, which has the periodicity of the magnetic lattice. Since the survival or decay of a He* atom depends on the relative orientation of the He* atom spin Σ to the local electron spin $\boldsymbol{S}(\boldsymbol{R})$ of a surface magnetic ion at $\boldsymbol{R}$, we can write ΔV^S in terms of the averaged scalar product of the spins $\langle \hat{\boldsymbol{\Sigma}} \cdot \hat{\boldsymbol{S}}(\boldsymbol{R}) \rangle$ as

$$\Delta V^S(\boldsymbol{r}) = C_0 \mathcal{M}_{Aug} \mathcal{D}_S(\boldsymbol{R}; z) \langle \hat{\boldsymbol{\Sigma}} \cdot \hat{\boldsymbol{S}}(\boldsymbol{R}) \rangle \tag{2}$$

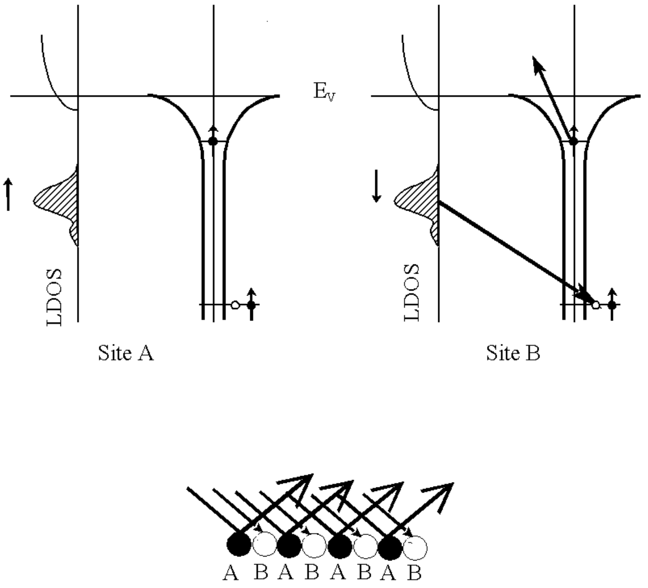

Figure 2. Spin-dependent enhancement of the local survival probability of a He* beam.

where $\mathcal{D}_S(\boldsymbol{R}; z)$ is the spin-dependent surface LDOS. We use the convention $\boldsymbol{r} \equiv (\boldsymbol{R}, z)$, where $\boldsymbol{R}$ is a vector parallel to the surface plane. Since in this picture both spins enter as non-interacting parameters and not as dynamical variables, we have $\langle \hat{\boldsymbol{\Sigma}} \cdot \hat{\boldsymbol{S}}(\boldsymbol{R}) \rangle = \langle \hat{\Sigma} \rangle \cdot \langle \hat{\boldsymbol{S}}(\boldsymbol{R}) \rangle$. With $\langle \hat{\Sigma} \rangle = 1/3$ for an unpolarized beam we obtain

$$\Delta V^S(\boldsymbol{r}) = \tfrac{1}{3} C_0 \mathcal{M}_{Aug} \mathcal{D}_S(\boldsymbol{R}, z) \langle \hat{S}_z(\boldsymbol{R}) \rangle. \tag{3}$$

This expression for the imaginary part of the potential allows us to use the thermal-averaged sublattice spin $\langle \hat{S}_z(\boldsymbol{R}) \rangle_T$, and, when convenient, express it in terms of a surface critical exponent β_1, as

$$\langle \hat{S}_z(\boldsymbol{R}) \rangle_T = S_0 \left(\frac{T_N^s - T}{T_N^s} \right)^{\beta_1} \tag{4}$$

where S_0 is the effective spin at 0 K, which is less than the value S due to zero-point energy fluctuations, T is the surface temperature and β_1 is a surface critical exponent. We then obtain

$$\Delta V^S(\boldsymbol{r}) = \frac{1}{3} C_0 \mathcal{M}_{Aug} \mathcal{D}_S(\boldsymbol{R}; z) S_0 \left(\frac{T_N^s - T}{T_N^s} \right)^{\beta_1}. \tag{5}$$

In general we express the total imaginary part of the potential as

$$V_I(\boldsymbol{r}) = \begin{cases} -\mathrm{i} V_0 \{1 + \xi(\boldsymbol{R}) \langle \hat{S}_z(\boldsymbol{R}) \rangle\} & \text{if } z_0 > z > 0; \\ 0 & \text{otherwise} \end{cases} \tag{6}$$

where $\xi(\boldsymbol{R}) = (\mathcal{D}_S(\boldsymbol{R}; z)/3\mathcal{D}_0)$, and z_0 is an effective range above the surface.

2.4. Modelling the He/surface Hamiltonian*

It was shown in [73] that the effective adiabatic Hamiltonian, obtained by integrating out the fast electronic degrees of freedom, is expressed as

$$\mathcal{H}_{\text{adiab}} = \frac{P^2}{2M} + V(\mathcal{R}) + v_M + v_P, \tag{7}$$

where $\mathcal{R}$ is the centre-of-mass (COM) coordinate of the He* atom, and P its COM momentum.

$$V(\boldsymbol{\mathcal{R}}) = V_R(\boldsymbol{\mathcal{R}}) + V_I(\boldsymbol{\mathcal{R}}), \tag{8}$$

is a complex, time-independent adiabatic scattering potential, with V_R and V_I having the geometric and magnetic periodicity, respectively. v_M is the magnetic interaction term

$$v_M = \sum_m J(|\boldsymbol{\mathcal{R}} - \boldsymbol{R}_m|)\boldsymbol{\Sigma} \cdot \boldsymbol{S}_m, \tag{9}$$

with $\boldsymbol{S}_m = \sum_i \boldsymbol{s}_{im}$; m labels the magnetic sites. Because $J(|\boldsymbol{\mathcal{R}} - \boldsymbol{R}_m|)$ is a function of $\boldsymbol{\mathcal{R}}$ it acts as an effective potential in the motion of the He*'s COM, thus allowing energy exchange between the surface electron-spin system and the COM of a He* atom. v_P is the phonon interaction term

$$v_P = \sum_j \nabla V_R(\boldsymbol{\mathcal{R}} - \boldsymbol{R}_j) \cdot \boldsymbol{u}_j, \tag{10}$$

where $\boldsymbol{u}_j$ is the displacement of the jth surface atom from its equilibrium position. Since its contribution to the magnetic properties is of higher order, we shall consider its effect only in terms of the Debye–Waller factor (DWF).

2.5. Aspects of the magnetic differential reflection coefficient (MDRC)

2.5.1. He diffraction intensities in the eikonal approximation.* In [9] we presented a detailed derivation of the MDRC for diffractive scattering associated with $V(\boldsymbol{\mathcal{R}})$ in the eikonal approximation. Treating $V_R(\boldsymbol{\mathcal{R}})$ as a corrugated hard-wall potential with corrugation function $\zeta(\boldsymbol{R})$, and $V_I(\boldsymbol{\mathcal{R}})$ as given in equation (6), we obtained the following expression for the diffraction amplitude, $\tilde{\mathcal{A}}_{\boldsymbol{G}}$, of the $\boldsymbol{G}$th channel:

$$\tilde{\mathcal{A}}_{\boldsymbol{G}} = \frac{\mathrm{e}^{-(W+\alpha)}}{\Omega} \int_{\substack{\text{primitive}\\ \text{mesh}}} \mathrm{d}\boldsymbol{R} \exp\{\mathrm{i}[\boldsymbol{G} \cdot \boldsymbol{R} + q_z \zeta(\boldsymbol{R})] - \xi(\boldsymbol{R})\langle \hat{S}_z(\boldsymbol{R})\rangle\}, \tag{11}$$

where Ω is the area of the surface primitive mesh, W the DWF and α is an attenuation factor accounting for an averaged He* beam decay through the PD channel [9].

In the case of the (2×1) spin-ordering, the diffraction amplitude of the 1/2-order peak was simply related to the SLM by

$$\mathcal{A}_{(1/2,0)} = \exp[-W - \alpha] I_1(\mathcal{B}\langle \hat{S}z(\boldsymbol{R})\rangle), \tag{12}$$

where $I_1(x)$ is the modified Bessel function of order 1, and $\mathcal{B}$ is a constant incorporating α and S_0. The first term in the expansion of $I_1(x)$ corresponds to the Born approximation:

$$\mathcal{A}^{\mathrm{Born}}_{(1/2,0)} \propto \exp\left[-W - \frac{\alpha}{\tilde{q}_z}\right]\left(1 - \frac{T}{T_N}\right)^{\beta_1}. \tag{13}$$

Thus, in keeping all the higher terms, we expect the eikonal approximation to yield a more accurate description of the scattering process. Similarly, the specular peak intensity is given by

$$\mathcal{A}_{(0,0)} = \exp\left[-W - \frac{\alpha}{\tilde{q}_z}\right] I_0(\mathcal{B}\langle \hat{S}_z(\boldsymbol{R})\rangle), \tag{14}$$

where $I_0(x)$ is the modified Bessel function of order 0.

2.5.2. Inelastic MDRC for He in the DWB approximation.* In [73] we focused on deriving the inelastic contribution to the MDRC in the DWBA framework. In this approach, the scattering by a simplified version of $V(\mathcal{R})$

$$V(\mathcal{R}) = V_0 \mathrm{e}^{\mathrm{i}\delta} \exp[-\alpha \mathcal{Z}], \tag{15}$$

was treated exactly, and the ensuing scattering wavefunctions were used to obtain the following expression for the corresponding inelastic MDRC:

$$\begin{aligned} \frac{\mathrm{d}^2 \Re(\boldsymbol{k}_f, \boldsymbol{k}_i)}{\mathrm{d}E_f \mathrm{d}\Omega} &= \left(\frac{1}{4\pi}\right)^2 \frac{2\Omega\alpha^2 S}{3\cos\theta_i} \left(\frac{J_0}{V_0}\right)^2 \frac{|\boldsymbol{k}_f|}{|\boldsymbol{k}_i|} |\mathcal{I}(p_{fz};\, p_{iz})|^2 \sum_{\boldsymbol{Q}} \mathcal{F}(\boldsymbol{Q}) \\ &= 2.1 \times 10^{-4} |\mathcal{I}(p_{fz};\, p_{iz})|^2 \frac{|\boldsymbol{k}_f|}{|\boldsymbol{k}_i|} \sum_{\boldsymbol{Q}} \mathcal{F}(\boldsymbol{Q}), \end{aligned} \tag{16}$$

where $J_0/V_0 = \sin\delta$, $\boldsymbol{k}_f$, $\boldsymbol{k}_i$ are the scattered and incident He* wavevectors, respectively, θ_i is the angle of incidence and Ω the surface unit mesh area. $\mathcal{I}(p_{fz};\, p_{iz})$ is a dimensionless form factor, and

$$\begin{aligned} \mathcal{F}(\boldsymbol{Q}) = n(\boldsymbol{Q})\delta\left\{\frac{\hbar^2}{2M}(k_f^2 - k_i^2) - \hbar\omega(\boldsymbol{Q})\right\}\delta(\boldsymbol{K}_f - \boldsymbol{K}_i - \boldsymbol{Q}) \\ + (n(\boldsymbol{Q}) + 1)\delta\left\{\frac{\hbar^2}{2M}(k_f^2 - k_i^2) + \hbar\omega(\boldsymbol{Q})\right\}\delta(\boldsymbol{K}_f - \boldsymbol{K}_i + \boldsymbol{Q})\Big] \end{aligned} \tag{17}$$

where $n(\boldsymbol{Q})$ is the thermal average of the occupation number of the $\boldsymbol{Q}$th spin excitation mode.

3. Experimental setup and procedures

3.1. Eperimental facility

Our experimental facility is comprised of two main components: a monochromatic He* beam generator and an ultra-high vacuum (UHV) scattering chamber. The first stage of the beam generator is a monochromator, based on a nozzle/skimmer assembly, which produces a monoenergetic beam of GS helium (He^0) atoms with energy resolution better than 1%. The second stage is the He* exciter [74], which is based on a coaxial excitation geometry. It is comprised of a high current electron gun of the Pierce type, equipped with a specially designed hemispherical matrix cathode. Electron beam axial confinement was achieved by either a specially designed solenoid or a three-stage electrostatic quadrupole. The implementation of time-of-flight (TOF) He* measurements was achieved by pulsing the excitation voltage, V_{acc}, applied to the e-gun, between $V_{\mathrm{acc}} < 19.8$ eV and $V_{\mathrm{acc}} \geqslant 20.3$ eV. The pulse duration is adjustable from 250 ns to 25 μs. The TOF system can be operated in a single-pulse mode or a crosscorrelation (psuedo-random binary) pulsed mode. Its operation is effected by a *digital signal processor*. The details of the design and operation are presented in [9, 74]. Beam intensities of about 10^6 He* atoms s^{-1} at the sample surface were achieved.

The UHV chamber houses two detectors: the He* detector consists of a channeltron electron multiplier and an angle-resolving aperture; it is exclusively sensitive to He* atoms, since it registers electron emission events associated with He* de-excitation. The He^0 detector consists of an electron gun with a crossed-electron–He^0 beam geometry and angle-resolving capability [75]. It produces a velocity-dispersed spatial distribution of He* atoms which is recorded on a position-sensitive electron channel plate [76]. The integrated output reflects the velocity-integrated intensity and the position-resolved intensity gives the velocity distribution of the angle-resolved scattered He^0 beam. The two detectors are mounted on a two-axis goniometer. Besides XYZ motions, and polar and azimuthal rotations, the sample manipulator is equipped with a Displex closed-cycle He refrigerator as well as a sample heater, allowing a change in the sample surface temperature in the range 30–600 K. The temperature controller (Scientific Instruments Inc. model 9600-1) is factory calibrated, and is accurate to ±0.5 K. The chamber is also equipped with traditional diagnostic, monitoring and sample preparation capabilities such as LEED/Auger spectrometers, RGA and a specially designed retractable UHV crystal cleaver.

3.2. General performance and characterization

Systematic characterization of the direct He* beam as a function of electron-impact excitation energy ($V_{\rm acc}$), and of stagnation temperature of the nozzle reservoir (T_0) was carried out, mainly by TOF measurements. $V_{\rm acc}$ determines the ratio of 2^1S to 2^3S metastable atoms in the beam, the intensity of the back-scattered beam and, to some extent, the beam's kinetic energy, which is mainly set by T_0. Typical TOF spectra at different excitation energies and reservoir temperatures are shown in figure 3. The peak at zero time, appearing in the TOF spectra for $V_{\rm acc} = 200$, 150 and 50 eV, is attributed to photons emitted in the excitation region, caused by radiative de-excitation, and was previously reported in [70, 77]. Radiative de-excitation occurs because high electron-impact energies give rise to excited states of He which can decay by emission of radiation. The zero-time peak is conspicuously absent in the $V_{\rm acc} = 20.5$ eV spectrum, as expected for electronic excitation energies where radiative decay is inhibited. Accordingly, our diffractive scattering measurements were always conducted with He* beams generated by $V_{\rm acc}$ in the range 20.3–20.5 eV. The peak that appears in figure 3 at about 260 μs for $T_s = 200$ K and at 220 μs for $T_s = 310$ K, and $V_{\rm acc} = 50$ eV, corresponds to a He* excitation process in which the impacting electron is back-scattered, while the prominent peak around 400 μs corresponds to forward-scattering of the impacting electron. The probability for back-scattering is dramatically reduced at high excitation energies, which accounts for the absence of this peak in the TOF spectrum for $V_{\rm acc} = 200$, and its appearance as a hardly recognizable shoulder at 150 eV.

Figure 4 presents results of a detailed study of the dependence of the intensity of this photon peak on $V_{\rm acc}$; indicating its disappearance for $V_{\rm acc} < 23$ eV. Figure 5 summarizes the dependence of the He* beam velocity on $V_{\rm acc}$ and T_s. Whereas TOF spectra of figure 3 were obtained with a nozzle-aperture $d_N = 20\,\mu$, figure 6 shows a typical TOF spectrum obtained with $d_N = 10\,\mu$, which displays a split forward-scattering peak due to a resonance excitation transfer collision from one He atom to another, first reported by Haberland and co-workers. Our results indicate that this process is indiscernible, within the resolution of our system, for $d_N = 20\,\mu$.

3.3. Sample preparation and measurement procedures

NiO and CoO crystalline samples were oriented and cut into rods approximately $8 \times 3 \times 4$ mm^3, with the long axis parallel to a $\langle 100 \rangle$ direction, and with transverse cleavage grooves spaced 2 mm apart. Each rod yielded two cleaves, on average. All of the data were obtained from surfaces freshly cleaved in vacuum, with a background pressure $<10^{-10}$ Torr with the He beam turned off. Silver conducting epoxy was used to attach an iron–constantan thermocouple to the sides of the rods at the location of the last cleavage groove. Scans were taken at 1 K increments near the bulk Néel temperature, and at larger increments at low temperatures. The temperature was controlled to within ±0.5 K during any scan. Measurements of (1/2, 0) diffraction intensity for NiO(001) consistently yielded $T_N^s = 529$ K for all cleaved surfaces, irrespective of their distance from the affixed thermocouple. After the first cleave the sample surface was about 2.0–2.5 mm away from the thermocouple, and after the second and final cleave the thermocouple was located precisely at the cleaved surface. T_N^b was determined by

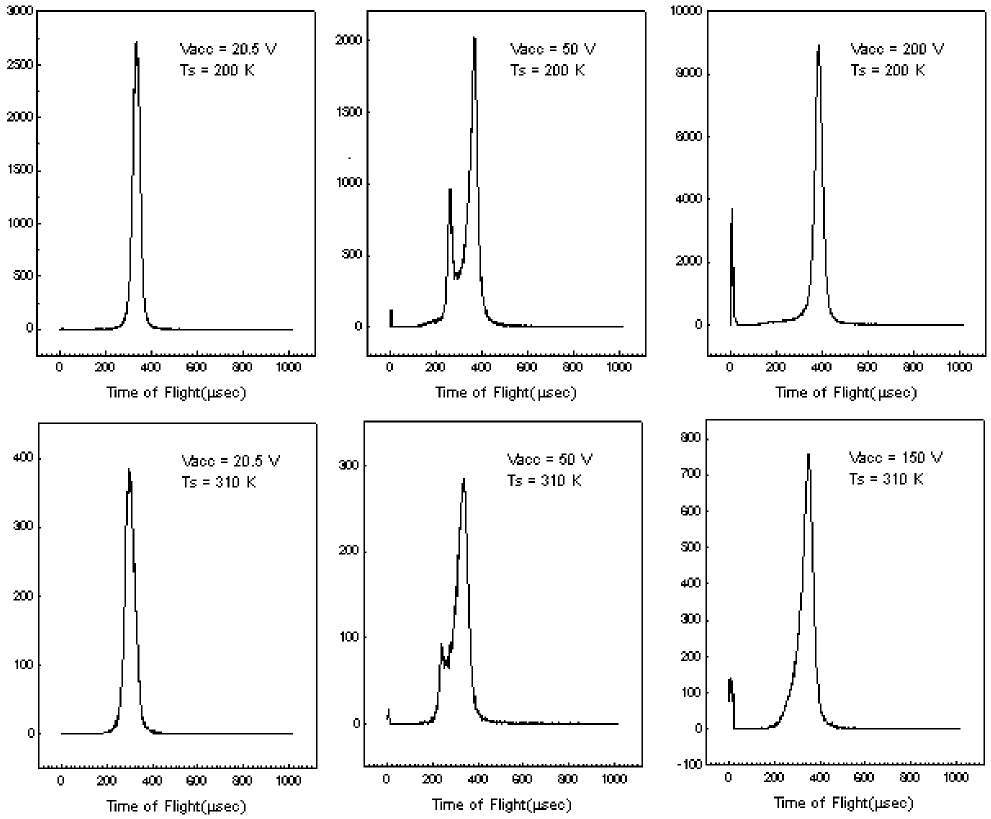

Figure 3. Typical TOF spectra of the direct He beam, measured at $T_s = 300$ and 200 K, and at different values of $V_{\rm acc}$.

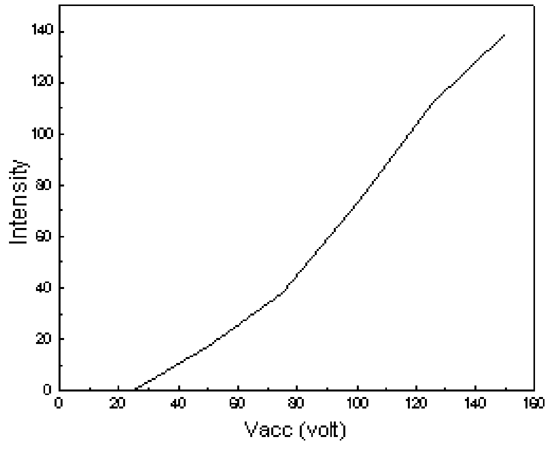

Figure 4. Dependence of the photon peak intensity on electron-impact excitation energy.

measuring the specific heat of several samples as a function of temperature with a Perkin–Elmer model DSC7 differential scanning calorimeter, which yielded $T_N^b = 523.6 \pm 0.2$ K for NiO, and $T_N^b = 290.0 \pm 0.2$ K for CoO.

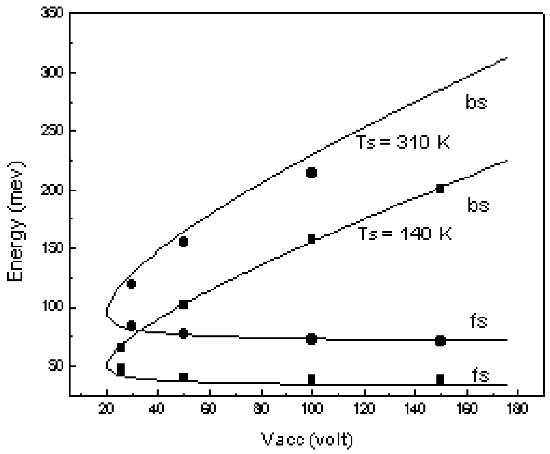

Figure 5. Dependence of the He* beam energy on electron-impact excitation energy, and on stagnation temperature. fs and bs stand for forward- and back-scattering.

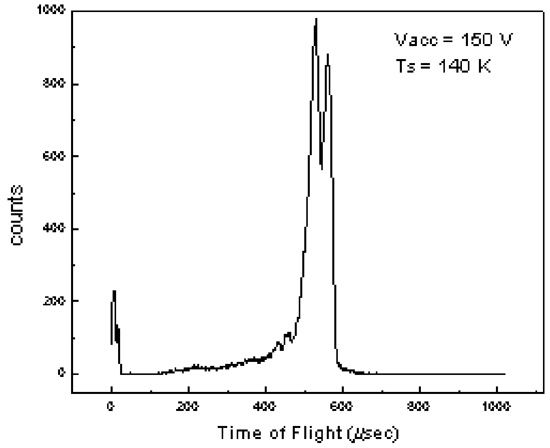

Figure 6. Typical TOF spectrum of the direct He*, measured at $T_s = 140$ K, nozzle aperture diameter 10 μ.

4. Magnetic critical behaviour at surfaces

Extensive studies of the magnetic critical behaviour at surfaces, carried out over the past 25 years [36, 39], have demonstrated that the universality classes associated with surface magnetic transitions are strongly dependent on the relative strengths of surface and bulk magnetic coupling, surface magnetic anisotropy [78] and surface symmetry. For the case of AFM phases, the universality class also depends on surface orientation [79]. In order to illustrate these concepts we consider the case of a semi-infinite Ising model, with lower critical dimension $d^* = 1$, in the absence of external fields.

Its phase diagram, figure 7, is depicted in terms of reduced exchange couplings $K_b = J_b/kT$, and $K_s = J_s/kT$, where T is the temperature, and J_b, J_s are the effective bulk and surface exchange couplings, respectively. The origin in figure 7 corresponds to infinite temperature. Paths 1, 2 and 3 represent the expected behaviour when the effective surface exchange coupling J_s is less than, greater than or equal to a critical value (J_s^c), respectively. When $J_s < J_s^c$ (path 1), the effective field at the surface is less than that in the bulk, suggesting (naively) that the surface might order at a *lower* temperature than the bulk. However, in this case, the bulk field is strong enough to force the surface to order passively at the bulk critical temperature, T_c^b. This critical behaviour, coined an *ordinary transition*, is characterized by

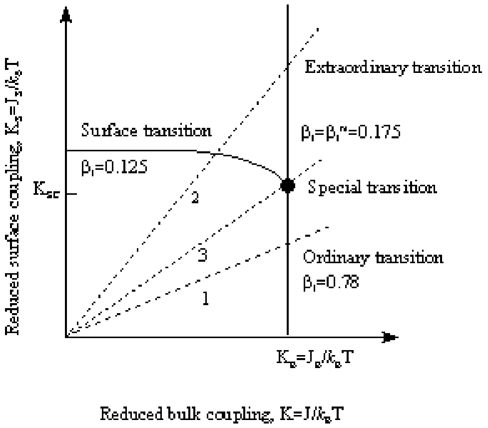

Figure 7. Phase diagram for a semi-infinite FM Ising system on a simple cubic lattice.

a surface magnetization critical exponent (SMCE) $\beta_1 = 0.78$–0.8 [33–35, 44, 45, 48]. When $J_s = J_s^c$ (path 3), the surface and bulk effective *critical* fields are comparable, and the two systems order independently at T_c^b. This *multicritical point*, called the *special transition*, is characterized by an SMCE $\beta_1 = \beta_1^m = 0.175$. Finally, in the case $J_s > J_s^c$ (path 2), the surface effective field is stronger than that of the bulk, and the surface orders at $T_c^s > T_c^b$, undergoing a pure two-dimensional 'surface transition', since the bulk is still in a paramagnetic state with a zero field. It should, therefore, be characterized by the SMCE $\beta_1 = 0.125$ corresponding to a two-dimensional Ising system. As the temperature of the system is lowered to the bulk critical temperature, we again have two independent critical fields, and as such this behaviour is described by the SMCE relevant to the multicritical point, $\beta_1 = 0.175$. This *crossover* from a two-dimensional to a multicritical behaviour was coined an *extraordinary transition* [46].

Binder and Landau (BL) studied the surface critical behaviour of the semi-infinite Ising system on a simple cubic lattice as a function of J_s/J_b, by extensive Monte Carlo (MC) simulations [33–35]. These studies revealed several important aspects: first, for values of $J_s/J_b < 1$ the SMCE was $\beta_1 \simeq 0.78$–0.8, consistent with an ordinary transition [44, 45, 48]. Second, the results obtained for $1.55 \leqslant J_s/J_b \leqslant 1.7$ revealed the presence of a crossover behaviour associated with the multicritical point. Introducing a two-dimensional Ising transition at a temperature $T_c^s > T_c^b$, with $\beta_1 = 0.125$, they obtained a critical value $J_s^c \simeq 1.52 J_b$. Moreover, a *crossover scaling function* $\tilde{m}_1^{SF}(x)$, in the neighbourhood of the multicritical point was determined, which describes the crossover from the surface transition to the extraordinary transition, at $T \leqslant T_c^b$,

$$m_1 = \tilde{m}_1^{SF}(x)\left(\frac{T_c^b}{T} - 1\right)^{\beta_1^m} \tag{18}$$

where the parameter x describes the dependence on J_S/J_s^c and $(T_c/T - 1)$:

$$x = \frac{|J_s/J_s^c - 1|}{(T_c^b/T - 1)^{\phi}} \tag{19}$$

with the crossover exponent $\phi = 0.56$. As shown in figure 8, the results obtained for J_s/J_b lg J_s^c collapsed on two branches when the reduced surface magnetization $m_1/m_0(T_N^b/T - 1)^{0.175}$ was plotted against the crossover scaling variable, $\left|J_s/J_{sc} - 1\right|/(523/T - 1)^{\phi}$ [33–35]. The upper branch corresponds to $J_s/J_b > J_s^c$ (path 2 in figure 6); while the lower branch corresponds to $J_s/J_b < J_s^c$ (path 1 in figure 7). The data corresponding to the multicritical point (path 3 in figure 7) fall on a horizontal line in this diagram. These results are universal in the sense that they hold for all anisotropic three-dimensional magnetic systems near T_c^b.

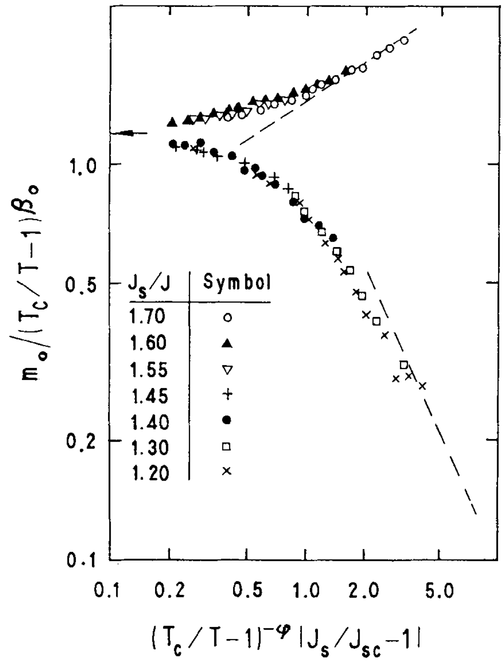

Figure 8. BL's data, collapsed onto the crossover function.

According to the well known Hohenberg–Mermin–Wagner theorem [80, 81], *for multicomponent order-parameter systems, $n > 1$, with $O(n), n > 1$ continuous symmetries* the lower critical dimension for the appearance of spontaneous order is $d_* = 2$, rather than $d_* = 1$ for the Ising systems ($n = 1$). Consequently, for such systems, such as the Heisenberg system, no two-dimensional surface, extraordinary or special transitions should take place. However, surface anisotropies may break the continuous symmetries of the $n = 3$ Heisenberg system, and an easy-magnetization axis may be favoured at the surface. Under these conditions, a surface transition akin to the Ising type may take place. Accordingly, there should be a multicritical point and, hence, anisotropic analogues of the special and extraordinary transitions. Yet, one expects that these transitions would belong to a different universality class from those associated with the Ising system. The multicritical transition associated with such surface anisotropies was studied, for the generalized case of d dimensions and $O(n)$ symmetry using renormalization-group methods [65], and labelled the surface 'anisotropic special' transition. The corresponding cross-over exponent was found to be $\simeq 0.57$, surprisingly close to that of the Ising system quoted above.

The NiO system has isotropic first- and second-neighbour exchange couplings. Moreover, because of the octahedral symmetry in the bulk, the spin–orbit-coupling site energies are isotropic and hence there is no site-anisotropy except for very weak dipolar interactions, as well as the slight distortions from the cubic structure that accompany the AFM phase. Although these anisotropies determine the magnetization direction, their magnitude is so small, $D_1 \simeq 0.1$ and $D_2 \simeq 0.006$ meV, that they are not expected to play a decisive role in determining the bulk Néel transition, $T_N^b = 523.6$ K. The NiO spin system in the bulk may, therefore, be classified as a Heisenberg system. However, as we shall show below, the reduction in symmetry at the surface gives rise to an appreciable uniaxial single-site anisotropy that places the critical behaviour of the surface in the anisotropic three-dimensional, $n = 3$ universality class.

5. Relevant properties of the 3d monoxides

5.1. Bulk properties

Magnetic neutron diffraction (MND) experiments showed that the AFM spin-ordering in these systems consists of AFM stacking of FM (111) planar sheets [11–17, 22, 25, 27]. Extensive experimental and theoretical studies of the exchange coupling in these oxides showed that nearest neighbour interactions J_1 are FM, of the overlap type, while next nearest neighbour couplings are J_2 are AFM, of the superexchange type [82, 83]; with $|J_2|/|J_1| \simeq 10$ [26].

In the paramagnetic (P) phase they have the NaCl structure ($Fm3m$, $\mathrm{O_h^5}$), whereas below T_N^b, the crystal becomes slightly distorted from the cubic structure; the distortion is rhombohedral for NiO and tetragonal for CoO [20]. This deformation is presumably due to the magnetostriction which accompanies the magnetic order: the amount of distortion is found to increase with decreasing temperature.

The magnetization direction of the FM (111) sheets in NiO is along the $\langle 11\bar{2}\rangle$, and is determined by the anisotropy of dipolar interactions among the spins [15, 16]. In CoO it lies out of the sheet plane and along the $\langle 113\rangle$ direction [84], which is determined by the spin–orbit (SO) splitting of the orbitally degenerate ground state (GS). Although early studies classified the AFM→P transition in NiO as first order [14], more recent MND results showed that the transition is second order [21]. The measured exponent $\beta = 0.33$ is close to both $\beta_{\mathrm{Ising}} = 0.325$ and $\beta_{\mathrm{Heisenberg}} = 0.345$. Similar studies of CoO indicated a similar behaviour [85–87].

Spin-wave dispersion curves (SWDCs) for NiO, measured by inelastic neutron scattering [26], reported a steep initial slope of ~250 meV Å, a maximum energy of ~117 meV and zone centre modes of 4.5 meV associated with out-of-the-(111)-plane anisotropy energy and a 1.5 meV mode associated with in-the-(111)-plane anisotropy energy. Empirical fits to the measured dispersion curves produced the following estimates: second-neighbour superexchange $J_2^b \sim 19.0$ meV, first-neighbour FM exchange $J_1^b \sim -1.37$ meV, out-of-plane site-anisotropy energy $D_1^b \sim 0.1$ meV, in-plane site-anisotropy energy $D_2^b \sim 0.006$ meV and an effective spin $\langle S\rangle_z \sim 0.9242$. SWDCs for CoO display a zone-centre gap of about 20 meV, as well as several excitonic branches at energies above 30 meV [84, 88–90]. Fits to the SWDCs yield $J_2 \simeq 2.4$ meV and $J_1 \simeq 0.25$ meV.

T_N^b for NiO is about 523 K, attributed, mainly, to $J_2 \simeq 19$ meV. By contrast, $T_N^b \simeq 290$ K for CoO cannot be attributed to $J_2 \simeq 2.4$ meV, and is mainly the result of a strong single-site anisotropy which is, in addition, manifested in the large gap found in the SWDCs.

5.2. Surface properties

Several experimental studies of the (001) surface structure of NiO and CoO, employing He^0 scattering, rule out the presence of surface lattice reconstruction [91–94], even around the Néel temperature, and report no discernible changes in surface phonon dispersions accompanying the transition [93–95]. Moreover, diffraction measurements showed that the effective surface corrugations are <0.14 Å [91].

The early LEED studies of Palmberg *et al* for NiO(001) reported a (2 × 1) surface magnetic structure, consistent with a bulk termination, and SMCE $\beta_1 = 1$, the mean-field value; however, their analysis did not correct for the surface DWF. Subsequently, Namikawa [96, 97] reported more detailed studies of the temperature dependence of the (1/2, 0) peak intensity, corrected for the DWF, which gave $\beta_1 \sim 0.89$, higher than the prediction for the Ising model (0.78–0.8) and the Heisenberg model (0.81), and below the mean-field value of 1. Consequently, no clear classification could be discerned, raising the question of the surface sensitivity of LEED with respect to the temperature dependence of surface spin-ordering. To our knowledge, there are no reports in the literature on the magnetic critical behaviour of CoO(001).

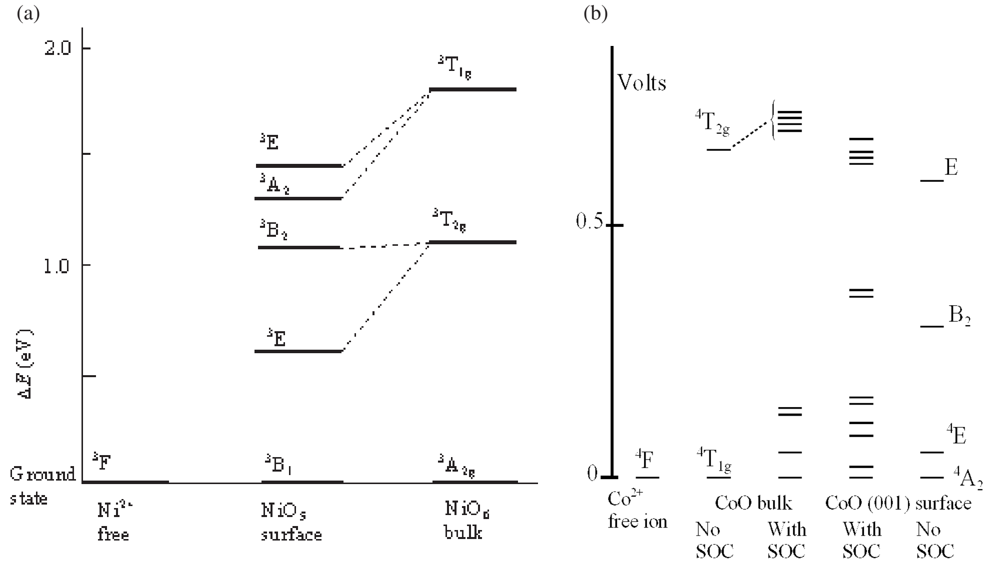

Figure 9. (a) NiO, (b) CoO. Schematic diagram of the electronic structure of (a) Ni^{2+} and (b) Co^{2+} in the free ion, the (001) surface and bulk.

5.3. Electronic structure and He scattering*

The ^3F ($3d^8$) GS of a free Ni^{2+} ion is split in bulk NiO by the octahedral symmetry of the crystal field (CF) into a non-degenerate $^3A_{2g}$ ($t_{2g}^6e_g^2$) GS, and two threefold degenerate excited states (ESs) $^3T_{2g}$ ($t_{2g}^5e_g^3$) and $^3T_{1g}$ ($t_{2g}^4e_g^4$, mixed with some $t_{2g}^5e_g^3$). The ^4F ($3d^7$) GS of a free Co^{2+} is split by bulk CF into a triply degenerate orbital GS, $^4\Gamma_4(^4T_{1g})$, with an effective orbital angular momentum $l = 1$, and Γ_5 and Γ_2 orbital ESs. The $^4\Gamma_4$ degeneracy is further reduced by SO interactions into a $j = 1/2$, doublet GS, and $j = 3/2, 5/2$ ES manifolds [18, 19].

Extensive electronic structure calculations using Hartree–Fock states with configuration interaction for a cluster model were carried out for both bulk and (001) surfaces of NiO [9, 98, 99] and CoO [100]. Bulk calculations confirmed earlier estimates of the energy splittings: for NiO the $^3T_{2g}$ and $^3T_{1g}$ ESs lie about 1.1 and 1.8 eV, respectively, above the $^3A_{2g}$ GS, while for CoO Γ_5 and Γ_2 are 0.67 and 1.48 eV, respectively, above $^4\Gamma_4$. The SO splitting for $j = 3/2$ and 5/2 was found to be 50 and 135 meV above the $j = 1/2$ GS, respectively. In addition the calculations yielded values of the exchange energies in good agreement with experimental values [73, 99]. The results of these calculations are shown in the schematic diagrams of figure 9. The lowering of symmetry to C_{4v} at the NiO(001) surface leads to a $^3B_1$ non-degenerate GS, with similar filling as the $^3A_{2g}$. The degeneracies of the two lowest ESs are partially removed with

$$^3T_{2g} \rightarrow \begin{cases} ^3E & (0.60\ \text{eV}) \\ ^3B_2 & (1.10\ \text{eV}) \end{cases} \qquad ^3T_{1g} \rightarrow \begin{cases} ^3A_2 & (1.30\ \text{eV}) \\ ^3E & (1.44\ \text{eV}) \end{cases}$$

where the numbers in parentheses are excitation energies from the GSs. These splittings are shown in the schematic diagram of figure 9. The $^3B_2$ ES corresponds to the excitation $3d_{xy} \rightarrow 3d_{x^2-y^2}$ and is not affected by the missing O^{2-} ion at the surface, whereas the ^3E, which corresponds to $3d_{xz} \rightarrow 3d_{z^2}$ and $3d_{yz} \rightarrow 3dz^2$ excitations, is lowered in energy. The configurations of the states splitting from $^3T_{1g}$ are more complicated.

Surface calculations reveal that the situation on the CoO(001) surface is quite different. As expected, the C_{4v} symmetry of the surface splits the Γ_4 states into nondegenerate A_2 and doubly degenerate E orbitals, and the Γ_5 states into B_2 and E orbitals. The effective CF splitting between A_2 and E is only 50 meV, comparable to SO interaction energies; hence, the latter cannot be treated as a mere perturbation on the CF state as was the case in the bulk. A properly balanced calculation shows that all the ensuing states are Kramers doublets. The first two ESs lie at 29 and 94 meV above the GS. Since both CF and SO interactions are treated on an equal basis the resulting states are not eigenstates of J, S or L. However, we find the expectation value of the spin in the GS and first ES to be $\langle s_z \rangle \simeq 1/2$ and $\langle s_z \rangle \simeq 3/2$, with z the normal to the surface. This assignment is confirmed when magnetic fields parallel and normal to the surface are introduced into the electronic structure calculations: in the former case the Zeeman splitting in the GS is larger than in the first ES, while in the latter case the reverse is true.

5.4. Magnetic coupling, anisotropies and spin Hamiltonians at the (001) surfaces

Two conflicting mechanisms affect the strength of the dominant superexchange coupling $J_{\mathrm{sup}} \equiv J_2$ at the (001) surfaces of 3d monoxides: the reduction in CF leads to an enhancement of J_{sup}, while the reduction in effective hopping, resulting from lower coordination number, favours a decrease in J_{sup}. Recent theoretical investigations reached contradicting and inconclusive results, ranging from an enhancement of 50% to a reduction of 20% [101, 102].

Moreover, the manifestations of single-site anisotropies (SSAs) are quite different in NiO and CoO, both in bulk and on the (001) surfaces. Because of the existence of nondegenerate GSs for NiO SSA is only effective in second-order perturbation and leads to an effective spin Hamiltonian of the form

$$\mathcal{H}_{ssa} = \sum_{ij} \Lambda_{ij} S_i S_j, \tag{20}$$

where Λ is the SO anisotropy matrix, and $S_{i,j}$ are the effective spin components. Λ is isotropic in the bulk because of octahedral symmetry. The C_{4v} symmetry at the (001) surface leads to $\Lambda_{zz} \equiv \Lambda_\perp \neq \Lambda_{xx} = \Lambda_{yy} \equiv \Lambda_\parallel$. Thus, apart from constant terms, we have $\Lambda_\perp$ and $\Lambda_\parallel$ such that the SSA Hamiltonian at the surface $\mathcal{H}^S_{ssa}$ is given by

$$\mathcal{H}^S_{ssa} = [\Lambda_\perp - \Lambda_\parallel] S_z^2 = D S_z^2. \tag{21}$$

Calculations based on the results of cluster models discussed above give $D \approx -2.5$ meV, so that $D/J_2^b \approx 0.13$ [9].

For CoO, the focus is mainly on the lowest lying manifold $^4F_{3/2}$. A model surface CF Hamiltonian, in the spin representation, is constructed with the aid of the operator equivalent formalism as [10]

$$\mathcal{H}_{CF} = a S_z^2 + b S_z^4 + c(S_+^4 + S_-^4). \tag{22}$$

Since $S^4_{+,-}$ are null operators for the $^4F_{3/2}$ subspace, $\mathcal{H}_{CF}$ splits this space into two doublets: $m_s = \pm 3/2$ and $\pm 1/2$ with an energy gap of $\Delta = 2a + 5b$, which is consistent with the results of the electronic cluster calculations, where the energy gap $\Delta = 29$ meV.

6. Results and discussion

Figures 10(a) and (b) show He* diffraction spectra measured at room temperature along the $\langle 10 \rangle$ direction for NiO and CoO, respectively, show the presence of 1/2-order peaks. Moreover, the fact that measurements along the $\langle 11 \rangle$ direction, presented in [9], show no sign of a (1/2, 1/2)-order peak, confirms that the surface electron spin-ordering is 2 × 1.

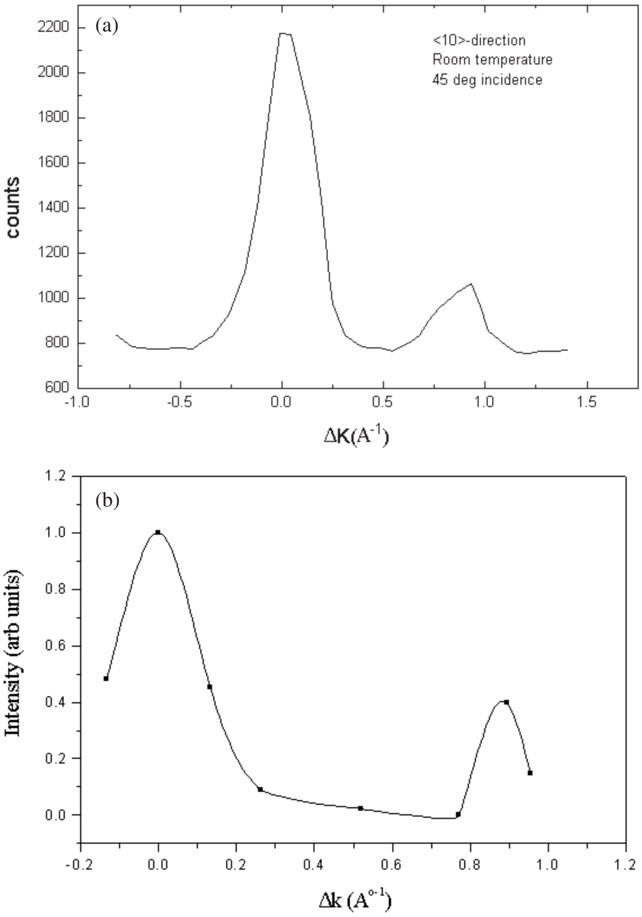

Figure 10. Diffraction spectra along the ⟨10⟩-direction of (a) NiO(001) and (b) CoO(001).

6.1. NiO(001)

Measurement of the (0, 0) and (1/2, 0) peak intensities were carried out for NiO(001) in the temperature range 300–536 K. The results are shown in figure 11. The width of the points reflects the experimental uncertainty in the measured intensity. The solid curves are a least-squares fit to the data using

$$\begin{aligned}
\frac{\mathcal{I}_{(0,0)}}{\mathcal{I}_{\mathrm{inc}}} &= \mathcal{A}^*_{(0,0)}\mathcal{A}_{(0,0)} = \exp[-2(W+\alpha)][I_0(\mathcal{B}\langle\hat{S}_z(\boldsymbol{R})\rangle)]^2, \\
\frac{\mathcal{I}_{(1/2,0)}}{\mathcal{I}_{\mathrm{inc}}} &= \mathcal{A}^*_{(\pi/a,0)}\mathcal{A}_{(\pi/a,0)} = \exp[-2(W+\alpha)][I_1(\mathcal{B}\langle\hat{S}_z(\boldsymbol{R})\rangle)]^2,
\end{aligned} \tag{23}$$

where $\mathcal{I}_{\mathrm{inc}}$ is the intensity of the incident beam. The data clearly indicate a $T_N^s = 529 \pm 1$ K, compared with $T_N^b = 523.6$, measured by calorimetry. The specular intensity, $\mathcal{I}_{(0,0)}$, approaches a non-zero magnitude above T_N^s, in agreement with the prediction of equation (14), and the fact that a non-magnetic contribution to the specular peak is expected to be present. By taking the ratio of the measured intensities, $\mathcal{I}_{(1/2,0)}/\mathcal{I}_{(0,0)}$, the factor $e^{-2(W+\alpha)}$ is eliminated,

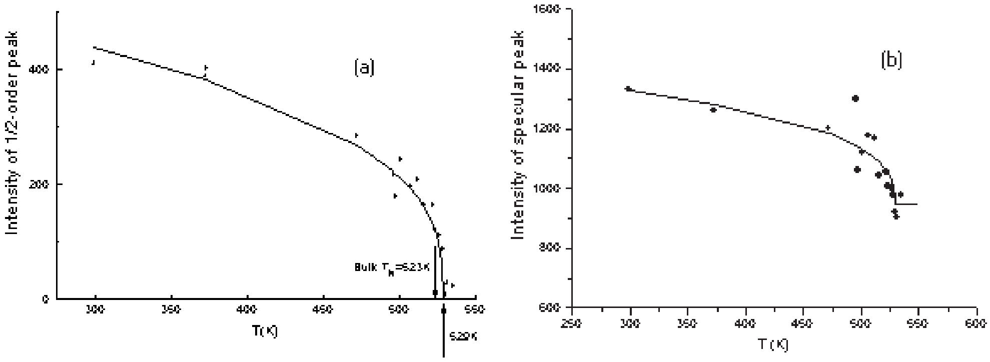

Figure 11. Temperature dependence of the (a) (0, 0); (b) (1/2, 0) intensity, showing $T_N^s = 529 \pm 1$, $T_N^b = 523$ K indicated by arrows. Solid symbols are experimental data, while the solid curves are $\propto I_1^0(x)$ and $I_1^2(x)$ fitted to the first and last experimental points.

and we obtain $B(T/T_N) = \mathcal{B}\langle \hat{S}_z(\boldsymbol{R}\rangle$ from the ratio

$$\mathcal{R}(T) = \sqrt{\frac{\mathcal{I}_{(1/2,0)}(T)}{\mathcal{I}_{(0,0)}(T)}} = \frac{I_1(B)}{I_0(B)}. \tag{24}$$

Further details of this procedure are given in [9].

Figure 12(a) shows a plot of

$$\ln B = \ln \mathcal{B} + \beta_1 \left[1 - \left(\frac{T}{T_N} \right) \right] \tag{25}$$

against $\ln[1 - (T/T_N^b)]$, $T_N^b = 523.6$ K. The apparent critical exponent for the surface SLM obtained from this plot (i.e. the slope of the best-fit line to the data) is 0.107 ± 0.014, which is unphysical since it is smaller than $\beta_1 = 0.125$ for the two-dimensional Ising system.

In figure 12(b), we repeat the same plot using instead $T_N^s = 529$ K. The two dotted lines indicate the expected asymptotic behaviour above and below $T_N^b = 523.6$ K for a system undergoing surface and extraordinary transitions: below T_N^b the system should exhibit multicritical behaviour asymptotically, characterized by the critical exponent 0.175.

Above T_N^b, the system should asymptotically exhibit behaviour corresponding to the surface transition, with a critical exponent of 0.125. While it is clear that more data are needed in the latter regime, the data below $T_N^b = 523.6$ fit a slope of 0.175. Figure 13 shows a plot of the reduced surface magnetization $B/(T_N^b/T - 1)^{0.175}$ against the crossover scaling variable, $|J_s/J_{sc} - 1|/(523.6/T - 1)^{\phi}$, with $\phi = 0.57$, the crossover exponent [65], and $|J_s/J_{sc} - 1| = 0.08$ obtained from the scaling relation

$$\frac{J_s}{J_{sc}} - 1 \propto \left(\frac{T_N^s}{T_N^b} - 1 \right)^{\phi} \tag{26}$$

of BL [33–35] using our experimental value of $T_N^s = 529$. The dashed line is the linear asymptote with slope 0.31. The data clearly indicate a monotonically increasing crossover scaling function, quite similar to the upper branch of the surface crossover function obtained by BL for the Ising model, which corresponds to the extraordinary transition. This is not surprising since the crossover scaling exponent derived by BL for the three-dimensional Ising model is $\phi = 0.56$. We, therefore, conclude that the three-dimensional Heisenberg model with surface anisotropy exhibits an anisotropic extraordinary transition with a critical behaviour very similar to that of the three-dimensional Ising model. Moreover, we ascertain that the

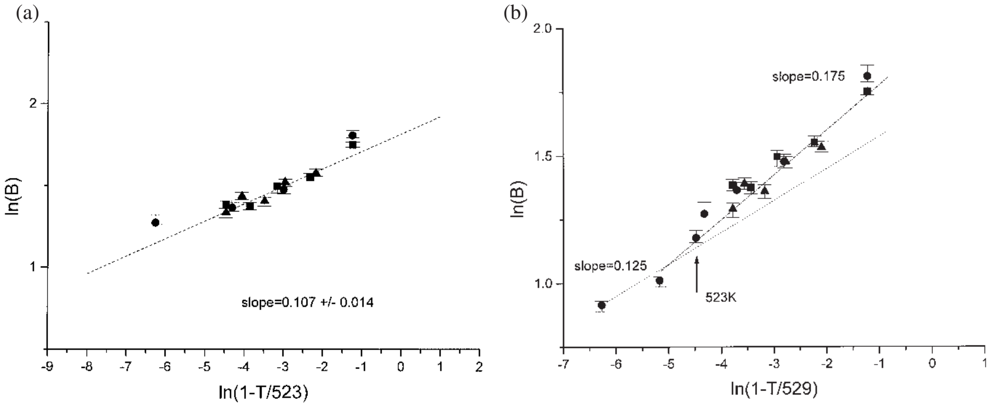

Figure 12. He* diffraction data fit to (a) bulk critical temperature and (b) observed critical temperature.

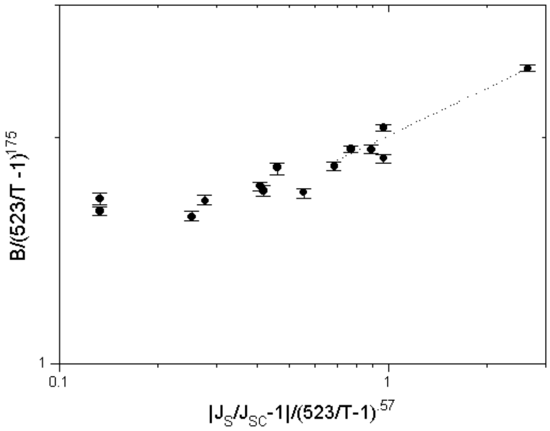

Figure 13. Crossover scaling of reduced magnetization as a function of the scaling variable $|J_s/J_{sc} - 1|(523/T - 1)^{-0.57}$, $J_s^{\text{eff}}/J_{sc} = 1.08$. The dashed line is the expected asymptotic behaviour with a slope of 0.31.

manifestation of this behaviour in our experimental data for the NiO(001) surface strongly supports and conforms with the enhanced T_N^s we obtain. We infer from these findings that the SLM of NiO(001) undergoes a surface transition at 529 K, and an extraordinary transition at $T_N^b = 523.6$ K. To our knowledge, this is the first observation of an extraordinary transition.

Recent studies of the (001) surface and bulk of the type II rock-salt antiferromagnets [103], based on the Schwinger boson mean-field (SBMF) method, indicate that the scenario of $T_N^s > T_N^b$ does not require $J_2^s > J_2^b$. Using a four-layer model with $J_1/J_2 = 0.1$, and a surface SSA D, $D/J_2^s = 0.1$, consistent with experimental values, yields $T_N^s = 3.85J_2^s$ and $T_N^b = 2.85J_2^b$. A nice feature of this SBMFT calculation is that the mean-field GS is disordered at any temperature if the site anisotropy is $D = 0$, thus preserving an important aspect of the physics. The predictions of SBMFT suggest that for $D/J_2^s = 0.1$ and the experimentally observed ratio $T_N^s/T_N^b = 1.012$ the surface coupling J_2^s should be $0.75J_2^b$, i.e. $J_2^s \simeq 15$ meV, compared with a bulk coupling of 19 meV.

When considering both the experimental and theoretical results presented above, we arrive at the following conclusions. The presence of SSA at the NiO(001) surface leads to an Ising-like critical behaviour, although in the strict sense this behaviour belongs to the universality classes of the anisotropic special and extraordinary transitions. If we take this similarity at face value, we infer from the experimental results that the effective surface magnetic exchange

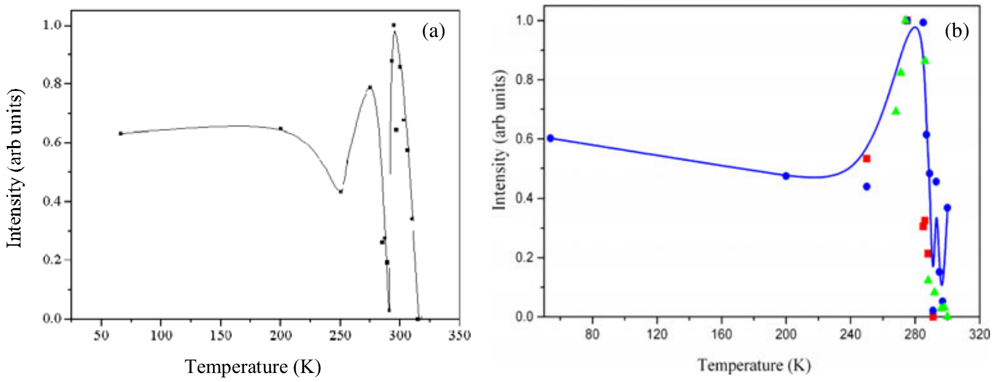

Figure 14. Temperature dependence of the $(1/2, 0)$ peak intensity.

coupling is about $J_2^s|_{\text{eff}} \approx 1.08 J_s^c = 1.6 \rightarrow 1.7 J_2^b$, when we use the critical exchange coupling value of BL. The moral inferred from the SBMF calculations is that such enhancements in the effective Ising-type surface exchange coupling are readily achieved by the presence of the site anisotropy at the surface, even when the actual J_2^s is lower than J_2^b.

6.2. CoO(001)

In figure 14 we show the temperature dependence of the $(1/2, 0)$ peak intensity. Figure 14(a) displays an enhancement of the peak intensity below and above $T_N^b = 290$ K; it represents data collected from a single cleave. Figure 14(b) shows more details of the enhancement below T_N^b, it depicts data collected from several cleaves. First, we notice that the peak intensity decreases slightly with increasing temperature from 50 to about 250 K. It then exhibits an anomalous increase with further increase in temperature, reaching a maximum at about 280 K followed by a steep decrease, reaching a minimum at T_N^b. Above T_N^b it increases once more to a maximum at 310 K and finally disappearing at about 320 K. This behaviour has been repeatedly checked, and was always reproducible even for different crystal ingots.

The model Hamiltonian for the two-dimensional square lattice can be written as

$$\mathcal{H} = \sum_{\alpha,\beta} \left[\mathcal{H}_{CF}^{\alpha} + \mathcal{H}_{CF}^{\beta} - J_1 \sum_{\langle nn \rangle} (\boldsymbol{S}_\alpha \cdot \boldsymbol{S}_\beta + \boldsymbol{S}_\alpha \cdot \boldsymbol{S}_{\alpha'} + \boldsymbol{S}_\beta \cdot \boldsymbol{S}_{\beta'}) + J_2 \sum_{\langle nnn \rangle} \boldsymbol{S}_\alpha \cdot \boldsymbol{S}_\beta \right], \tag{27}$$

where α, β index the two different AFM sublattices.

We evaluate the free energy of the system using the Bogolyubov–Peierls mean-field variational method [104, 105], using a noninteracting Hamiltonian of the form

$$\mathcal{H}_0 = \sum_{\alpha} (\mathcal{H}_{CF}^{\alpha} - h_\alpha S_\alpha^z) + \sum_{\beta} (\mathcal{H}_{CF}^{\beta} - h_\beta S_\beta^z), \tag{28}$$

where $h_{\alpha,\beta}$ are the effective mean fields along the z-axis, taken as variational parameters. The temperature dependence of the SLM is then determined from the self-consistent equation

$$M = \frac{1}{2} \frac{\sinh(2jtM) + 3\exp[-t]\sinh(6jtM)}{\cosh(2jtM) + \exp[-t]\cosh(6jtM)}, \tag{29}$$

where $j = J_2/\Delta$ and $t = \Delta/k_B T$. The computed $M(T)$ is used to determine the 1/2 order peak intensity, shown in figure 15, using equation (29). It exhibits three regimes: for $j \leqslant 0.25$, the saturation magnetization is $M = 0.5$ per site, and the behaviour at high temperatures is normal mean-field-like; a similar behaviour is obtained for $j > 0.32$ except that the saturation magnetization assumes the value $M = 1.5$ per site. For the range $0.25 < j < 0.32$ the system

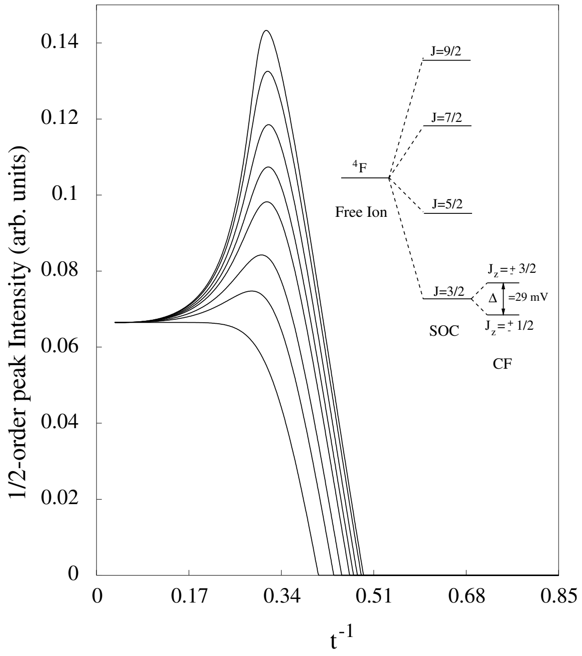

Figure 15. Temperature dependence of the magnetization for $0.25 \leqslant j \leqslant 0.32$.

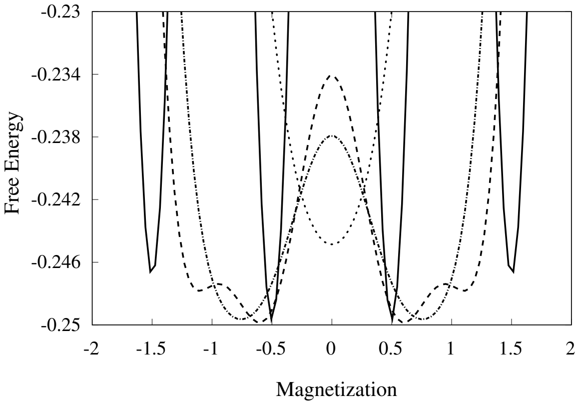

Figure 16. Typical free energy per site $f(M)$ for $0.25 < j < 0.32$, at low T (solid), T in enhanced range (dashed), at peak enhancement (dash–dotted) and at $T > T_N$ (dotted).

exhibits an anomalous peak manifesting the temperature-induced magnetization. Examination of the free energy per site, f, reveals the nature of the temperature-induced enhancement of the sub-lattice magnetization. Figure 16 shows typical behaviour of f as a function of the magnetization at several temperatures: for T below the enhancement range, we observe minima at $M = \pm 0.5$ and at ± 1.5, with absolute minima at ± 0.5. However, when T is within the enhancement range each of the positive and negative pairs of minima move toward each other, with the absolute minimum being the one closer to $|M| = 0.5$. At the temperature corresponding to peak magnetization each pair merges, then, with increasing temperature, the ensuing minima start to move toward $M = 0$, ultimately reaching it at the Néel temperature, thus giving rise to the paramagnetic phase.

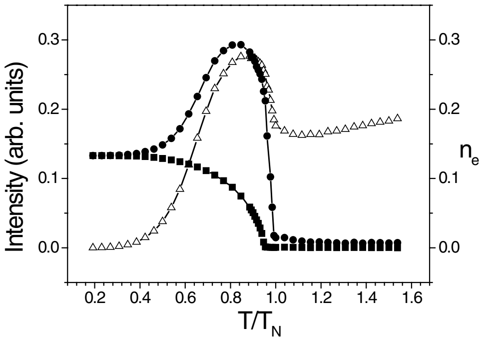

Figure 17. MC results for the temperature dependence of the $(1/2, 0)$ peak intensity: bulk (solid squares), surface (solid circles); and of the surface excited-state population n_e (open triangles).

In order to investigate the effect of thermal fluctuations and of surface–bulk coupling, and, possibly, to determine the origin of the suppression of the AFM surface ordering in the neighbourhood of T_N^b, we carried out MC simulations based on slab geometries, and on a Hamiltonian of the form

$$\begin{aligned} H &= H_s + H_{sb} + H_b \\ H_\alpha &= J_\alpha \sum_{\langle nnn\rangle} \vec{S}_i^\alpha \cdot \vec{S}_j^\alpha + \frac{\Delta^\alpha}{2} \sum_i (S_{iz}^\alpha)^2 \\ H_{sb} &= J_{sb} \sum_{\langle nnn\rangle} \vec{S}_i^s \cdot \vec{S}_j^b \end{aligned} \tag{30}$$

where s and b refer to surface and bulk, respectively, and $\alpha = s$ or b. We show typical results in figures 17 and 18, for a $100 \times 100 \times 101$ slab with periodic boundary conditions, and for $J_s = 0.25\Delta^s$, $J_b = 0.22\Delta^s$, $J_{sb} = 0.2\Delta^s$ and $\Delta^b = 1.67\Delta^s$. Figure 17 shows the diffraction intensities of the surface and bulk magnetic peaks as a function of reduced temperature. The bulk spins do not populate the $\pm\frac{3}{2}$ manifold, since the energy gap is much higher than T_N^b; and the bulk magnetic intensity exhibits a power law critical behaviour with a critical exponent $\beta = 0.322 \pm 2$, consistent with the exact value of 0.325 for the Ising system. The surface M manifests an anomalous peak, similar to both experimental and mean-field results. It also shows that $T_N^s > T_N^b$. The lower panel of figure 5 depicts the population of the excited state n_e, which peaks at the same temperature as the magnetization. n_e is appreciably higher than would be expected from thermal activation across Δ^s. As the surface approaches its Néel temperature, the entropy-driven population of the GS resumes, signalling a re-entrance process.

Figure 18 shows surface spin configurations at different surface temperatures. The stripe character in these figures is a manifestation of the 2×1 surface-spin ordering. At low temperatures the GS is populated exclusively as indicated by the red/blue stripes. As the temperature is raised yellow/green stripes, representing the excited state population, appear. A coexistence of the two phases is observed. The grey areas in the last panel, $T > T_N^S$ represent the paramagnetic phase.

The following picture emerges from the results presented above: at low enough temperatures, the ordered AFM bulk spins pin down the surface spins to the $s_z = 1/2$ state. As the temperature increases, the bulk spin ordering decreases, and the surface spins, less constrained by the bulk, re-orient by populating the first $s_z = 3/2$ excited state. The reorientation arises because of two contributions to the free energy: the energy of the 3/2-state is lowered through coupling to surface neighbours $\sim S^2 J_s$, with $S = \pm\frac{3}{2}$, and the entropy is increased by populating new states. So far, no evidence of the 1/2-order peak attenuation at T_N^b has been observed in the MC calculations. One possible explanation is that the size of the slab may be inadequate to support long-wavelength bulk critical fluctuations which

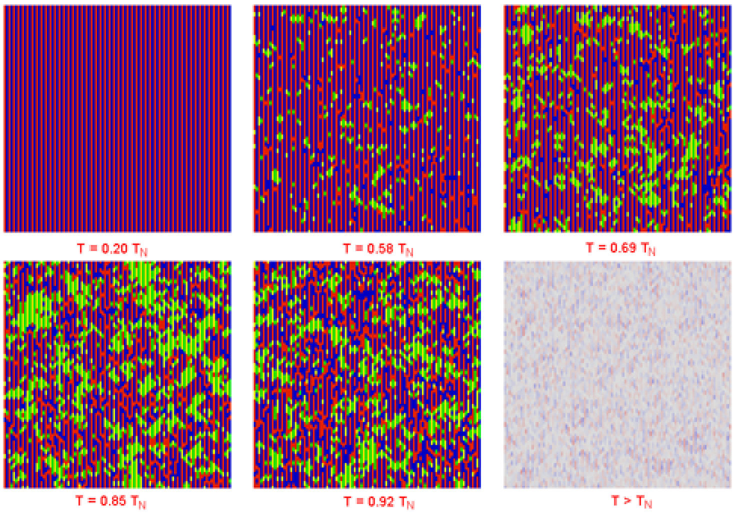

Figure 18. Configuration of the surface spin system at different temperatures. $s_z = \pm 1/2$, red/blue, $s_z = \pm 3/2$, yellow/green.

may be necessary to increase surface disorder; another is that proper choice of the effective surface–bulk coupling has to be found. Currently, work on these aspects is still in progress.

6.3. Inelastic scattering from CoO(001)

I would like to conclude this review with the unfinished work concerning He* TOF spectra obtained for CoO(001), at a surface temperature of 50 K. These spectra reveal the presence of inelastic events in the excitation energy range 30 meV $\geqslant \hbar\omega \leqslant$ 60 meV. These excitations were not reported in phonon studies of this surface [93, 94]. He-scattering measurements only captured modes below 30 meV, while surface optical phonon events, above 30 meV were obtained by electron energy loss spectroscopy.

Typical TOF spectra collected at $\theta_i = 42°$, $E_i = 72$ meV, and at different scattering angles along the [10]-direction are shown in figure 19. In order to achieve the high beam intensities required for TOF measurements, the He* beam used was generated with electron excitation energies of 150 eV. Singlet 2^1S atoms were, therefore, present. Detailed studies of the peak fixed at 300 μs demonstrated that it arises from photons emitted at the CoO(001) surface, which are associated with a *Stark-like* decay channel of the metastable singlet atoms. It provides an interesting marker for determining the flight time from the sample surface to the detector. Because we used a gating time of 30 μs, and electron excitation energy of 150 V, the zero-time light peak now spans the first 30 μs of the TOF spectra, with a maximum at approximately 20 μs. In figure 19(a) two peaks appear at 390 and 500 μs, and are seen to disperse towards each other, progressively, on going from spectrum (b) to (g) and, ultimately, merge into one single peak at 450 μs. The dispersion of these two peaks extends over the range 40–60 meV and does not conform with the surface phonon dispersion curves calculated in [94] to fit the experimental data along the $\langle 100\rangle$-$\bar{\Gamma}\bar{\mathrm{X}}$ direction. This seems to indicate that the inelastic events in the He* TOF spectra are not manifestations of surface phonon events. Moreover, bulk CoO possesses a very strong single-site anisotropy; one of its manifestations is the appearance of an appreciable gap (>20 meV) at $q = 0$ in the bulk spin wave dispersion, as measured by inelastic neutron scattering [88, 89].

Moreover, the lowest bulk magnon dispersion curve extends from 20 meV up to energies

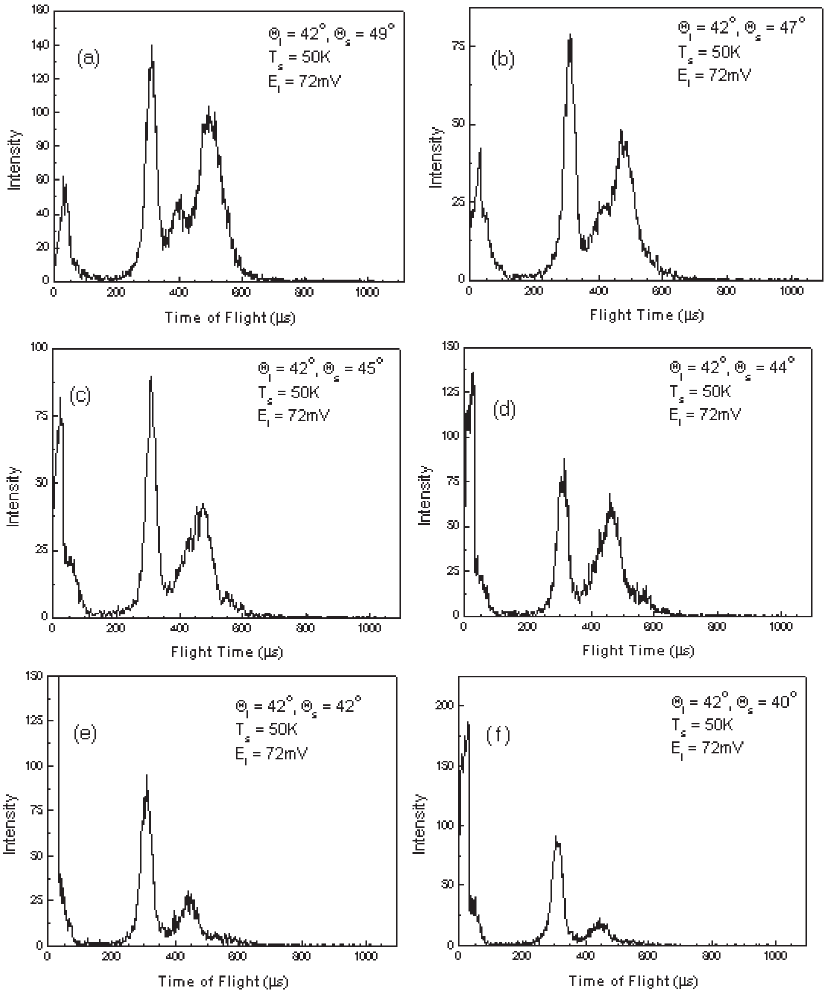

Figure 19. Typical TOF spectra obtained with He* beam energy of 72 eV, 42° angle of incidence, for CoO(001) at 50 K along the ⟨10⟩ direction.

of about 40 meV, while two higher spin excitation branches, associated with magnetic excitons, appear at about 45 and 56 meV [89]. It is quite likely, therefore, that the He* data are manifestations of magnetic-exciton bands. The modelling and analysis of these data are being now considered in the light of the new model of the CoO(001) spin system.

Acknowledgments

The author would like to acknowledge his collaborators without whom this work could never have been accomplished. He is indebted to Professor V Staemmler and his group, for using their expertise in carrying out the elaborate electronic cluster calculations which were crucial to understanding all the experimental results discussed above. He is also indebted to his former student M Marynowski for the NiO work, and to his current students P Banerjee, X-F Liu and M Farzaneh for discovering the CoO anomaly and their invaluable contributions toward revealing the physics behind it. This work is supported by the US Department of Energy under grant No DE-FG02-85ER45222.

References

[1] Hulpke E (ed) 1992 *Helium Atom Scattering* (Berlin: Springer)
[2] Benedek G and Toennies J 1994 *Surf. Sci.* **299/300** 587
[3] Garibaldi U, Levi A, Spadacini R and Tommei G 1973 *Surf. Sci.* **38** 269
[4] Garibaldi U, Levi A, Spadacini R and Tommei G 1975 *Surf. Sci.* **48** 649
[5] Schiff L 1970 *Quantum Mechanics* 2nd edn (New York: McGraw-Hill) ch 37
[6] Manson R and Celli V 1971 *Surf. Sci.* **24** 495
[7] Cabrera N, Celli V and Manson R 1969 *Phys. Rev. Lett.* **22** 346
[8] Cabrera N, Celli V, Goodman F and Manson R 1970 *Surf. Sci.* **19** 67
[9] Marynowski M, Franzen W, El-Batanouny M and Staemmler V 1999 *Phys. Rev.* B **60** 6053
[10] Banerjee P *et al Phys. Rev. Lett.* submitted
[11] Shull C, Strauser W and Wollan E 1951 *Phys. Rev.* **83** 333
[12] Roth W 1958 *Phys. Rev.* **110** 1333
[13] Roth W 1958 *Phys. Rev.* **111** 772
[14] Roth W 1960 *J. Appl. Phys.* **31** 2000
[15] Yamada T 1966 *J. Phys. Soc. Japan* **31** 664
[16] Yamada T, Saito S and Shimomura Y 1966 *J. Phys. Soc. Japan* **21** 672
[17] Uchida E *et al* 1967 *J. Phys. Soc. Japan* **23** 1197
[18] Kanamori J 1957 *Prog. Theor. Phys.* **17** 177
[19] Kanamori J 1957 *Prog. Theor. Phys.* **17** 197
[20] Rooksby H 1948 *Acta Crystallogr.* **1** 26
[21] Negovetić I and Konstantinović J 1973 *Solid State Commun.* **13** 249
[22] Nagamiya T, Yosida K and Kubo R 1955 *Adv. Phys.* **4** 1
[23] Lines M E 1965 *Phys. Rev.* A **139** 1304
[24] Lines M E 1964 *Phys. Rev.* A **135** 1336
[25] Joshua S 1991 *Symmetry Principles and Magnetic Symmetry in Solid State Physics* (Bristol: Institute of Physics Publishing) ch 37
[26] Hutchings M and Samuelsen E 1972 *Phys. Rev.* 3447
[27] Cracknell A 1975 *Magnetism in Crystalline Materials* (Oxford: Pergamon)
[28] Mills D 1971 *Phys. Rev.* B **3** 3887
[29] Wolfram T, de Wames R, Hall W and Palmberg P 1971 *Surf. Sci.* **28** 45
[30] Binder K and Hohenberg P 1972 *Phys. Rev.* B **6** 3461
[31] Binder K and Hohenberg P 1974 *Phys. Rev.* B **9** 2194
[32] Binder K and Landau D 1976 *Surf. Sci.* **61** 577
[33] Binder K and Landau D 1984 *Phys. Rev. Lett.* **52** 318
[34] Binder K and Landau D 1990 *Phys. Rev.* B **41** 4633
[35] Binder K and Landau D 1990 *Phys. Rev.* B **41** 4786
[36] Binder K 1986 *Phase Transition and Critical Phenomena* vol 8, ed C Domb and J Lebowitz (London: Academic)
[37] Bray A and Moore M 1977 *Phys. Rev. Lett.* **38** 735
[38] Bray A and Moore M 1977 *J. Phys. A: Math. Gen.* **10** 1927
[39] Diehl H 1988 *Phase Transition and Critical Phenomena* vol 10, ed C Domb and J Lebowitz (London: Academic)
[40] Diehl H and Dietrich S 1980 *Phys. Lett.* A **80** 375
[41] Diehl H and Dietrich S 1981 *Z. Phys.* B **42** 65
[42] Diehl H and Dietrich S 1981 *Phys. Rev.* B **24** 2878
[43] Diehl H and Dietrich S 1983 *Z. Phys.* B **50** 117
[44] Diehl H and Shpot M 1994 *Phys. Rev. Lett.* **73** 3431
[45] Diehl H and Shpot M 1998 *Nucl. Phys.* B **528** 595
[46] Lubensky T and Rubin M 1975 *Phys. Rev.* B **12** 3885
[47] Lubensky T and Rubin M 1973 *Phys. Rev. Lett.* **31** 1469
[48] Pleimling M and Selke W 1998 *Eur. Phys. J.* B **1** 385
[49] Palmberg P, de Wames R and Vredevoe L A 1968 *Phys. Rev. Lett.* **21** 682
[50] Palmberg P, de Wames R, Vredevoe L A and Wolfram T 1969 *J. Appl. Phys.* **40** 1158
[51] Lubensky T and Rubin M 1975 *Phys. Rev.* B **11** 4533
[52] Bray A and Moore M 1977 *Phys. Rev. Lett.* **38** 1046
[53] Alvarado S, Campagna M and Hopster H 1982 *Phys. Rev. Lett.* **48** 51
[54] Alvarado S, Campagna M, Ciccacci F and Hopster H 1982 *J. Appl. Phys.* **53** 7920
[55] Rau C and Eichner S 1980 *Nuclear Methods in Materials Research* ed K Bedge, H Bauman, H Jex and F Rauch

(Braunschweig: Vieweg) p 354
[56] Rau C 1983 *J. Magn. Magn. Mater.* **31–4** 874
[57] Weller D *et al* 1985 *Phys. Rev. Lett.* **54** 1555
[58] Tang H *et al* 1993 *Phys. Rev. Lett.* **71** 444
[59] Rau C, Jin C and Robert M 1988 *J. Appl. Phys.* **63** 3667
[60] Swan A, Franzen W, El-Batanouny M and Martini K 1991 *The Structure of Surfaces* vol 3, ed C Tong, M van Hove, and K Takayanagi (Berlin: Springer) p 190
[61] Swan A, Franzen W, El-Batanouny M and Martini K 1991 *MRS Symp. Proc. No 208* ed T Huang, P Cohen and D Eaglesham (Pittsburgh, PA: Materials Research Society) p 273
[62] Swan A *et al* 1993 *Phys. Rev. Lett.* **71** 1250
[63] Swan A *et al* 1994 *J. Vac. Sci. Technol.* A **12** 2219
[64] Marynowski M *et al* 1995 *Surf. Interface Anal.* **23** 105
[65] Diehl H and Eisenriegler E 1984 *Phys. Rev.* B **30** 300
[66] Locke J 1969 A critical evaluation of the metastable time-of-flight technique for obtaining molecular velocity distributions *UTIAS Report* p 143
[67] Van Dyke R S Jr, Johnson C and Shugart H 1971 *Phys. Rev.* A **4** 1327
[68] Sesselmann W *et al* 1987 *Phys. Rev.* B **35** 1547
[69] Conrad H *et al* 1982 *Surf. Sci.* **121** 161
[70] Conrad H *et al* 1982 *Surf. Sci.* **117** 98
[71] Hagstrum H 1977 *Inelastic Ion–Surface Collisions* ed N Tolk, J Tully and C White (New York: Academic) p 1
[72] Sesselmann W *et al* 1983 *Phys. Rev. Lett.* **50** 446
[73] El-Batanouny M *et al* 1998 *Phys. Rev.* B **58** 7391
[74] Marynowski M, Franzen W and El-Batanouny M 1994 *Rev. Sci. Instrum.* **65** 3718
[75] Martini K, Franzen W and El-Batanouny M 1987 *Rev. Sci. Instrum.* **58** 1027
[76] El-Batanouny M and Franzen W *Rev. Sci. Instrum.* submitted
[77] Fouquet P, Day P and Witte G 1998 *Surf. Sci.* **400** 140
[78] Czerner P and Ritschel U 1997 *Int. J. Mod. Phys.* B **11** 2075
[79] Drewitz A, Leidl R, Burkhardt T and Diehl H 1997 *Phys. Rev. Lett.* **78** 1090
[80] Hohenberg P 1967 *Phys. Rev.* B **158** 383
[81] Mermin N and Wagner H 1966 *Phys. Rev. Lett.* **17** 1133
[82] Anderson P 1950 *Phys. Rev.* **79** 350
[83] Anderson P 1987 *Science* **235** 1196
[84] Herrmann-Ronzaud D, Burlet P and Rossat-Mignod J 1978 *J. Phys. C: Solid State Phys.* **11** 2123
[85] Rechtin M, Moss S and Averbach B 1970 *Phys. Rev. Lett.* **24** 1485
[86] Rechtin M and Averbach B 1972 *Phys. Rev.* B **6** 4294
[87] Salamon M 1970 *Phys. Rev.* B **2** 214
[88] Sakurai J, Buyers W, Cowley R and Dolling G 1968 *Phys. Rev.* **167** 510
[89] Wagner V 1978 *J. Physique Coll.* **39** C6 822
[90] Wagner V and Herrmann-Ronzaud D 1978 *Proc. Symp. on Neutron Inelastic Scattering* (International Atomic Energy Agency)
[91] Cantini P, Tatarek R and Felcher G 1979 *Phys. Rev.* B **19** 1161
[92] Bishop G *et al* 1995 *J. Vac. Sci. Technol.* A **13** part 2 1416
[93] Toennies J, Witte G, Shikin A and Rieder K 1993 *J. Electron. Spectrosc. Relat. Phenom.* **64/65** 677
[94] Witte G, Senet P and Toennies J 1998 *Phys. Rev.* B **58** 13 264
[95] Brug W *et al* 1992 *J. Vac. Sci. Technol.* A **10** part 3 2222
[96] Namikawa K, Wolfram T, Hayakawa and Miyake S 1974 *J. Phys. Soc. Japan* **37** 733
[97] Namikawa K 1978 *J. Phys. Soc. Japan* **44** 165
[98] Fink K, Fink R and Staemmler V 1994 *Inorg. Chem.* **33** 6219
[99] Wang C, Fink K and Staemmler V 1995 *Chem. Phys.* **192** 25
[100] Staemmler V and Fink K *Chem. Phys.* submitted
[101] Pothuizen J, Cohen O and Sawatzky G 1996 *MRS Symp. Proc.* **401** 501
[102] de Graaf C, Broer R and Nieuwport W 1997 *Chem. Phys. Lett.* **271** 372
[103] Murthy G and Sharma P private communication, at press
[104] Feynman R 1998 *Statistical Mechanics* (Reading, MA: Addison-Wesley)
[105] Callen H 1985 *Thermodynamics and an Introduction to Thermostatistics* (New York: Wiley)